









Demonstration of valley anisotropy utilized to enhance the thermoelectric power factor

Airan Li ^{1,3}, Chaoliang Hu ^{1,3}, Bin He², Mengyu Yao ², Chenguang Fu ¹✉, Yuechu Wang ¹,
Xinbing Zhao ¹, Claudia Felser ² & Tiejun Zhu ¹✉

Valley anisotropy is a favorable electronic structure feature that could be utilized for good thermoelectric performance. Here, taking advantage of the single anisotropic Fermi pocket in p-type Mg_3Sb_2 , a feasible strategy utilizing the valley anisotropy to enhance the thermoelectric power factor is demonstrated by synergistic studies on both single crystals and textured polycrystalline samples. Compared to the heavy-band direction, a higher carrier mobility by a factor of 3 is observed along the light-band direction, while the Seebeck coefficient remains similar. Together with lower lattice thermal conductivity, an increased room-temperature zT by a factor of 3.6 is found. Moreover, the first-principles calculations of 66 isostructural Zintl phase compounds are conducted and 9 of them are screened out displaying a p_z -orbital-dominated valence band, similar to Mg_3Sb_2 . In this work, we experimentally demonstrate that valley anisotropy is an effective strategy for the enhancement of thermoelectric performance in materials with anisotropic Fermi pockets.

¹State Key Laboratory of Silicon Materials, School of Materials Science and Engineering, Zhejiang University, Hangzhou, China. ²Max Planck Institute for Chemical Physics of Solids, Dresden, Germany. ³These authors contributed equally: Airan Li, Chaoliang Hu. ✉email: chenguang_fu@zju.edu.cn; zhutj@zju.edu.cn

Thermoelectric (TE) devices, which convert heat into electricity or vice versa, exhibit promising applications in aerospace explorers as power generators, room-temperature refrigeration, and energy supply for the Internet of Things¹, etc. The conversion efficiency is governed by the dimensionless figure of merit zT of the used TE materials, $zT = S^2\sigma/(\kappa_L + \kappa_e)$, where S , σ , κ_L , and κ_e stand for Seebeck coefficient, electrical conductivity, lattice and electronic component of the thermal conductivity κ , respectively². The challenge in the enhancement of zT lies in that these transport parameters are not independent but coupled to one another. Among them, both the S and σ are dominated by the behavior of electrons near the Fermi level E_F . Increasing σ usually reduces absolute S . Therefore, how to decouple S and σ to realize a largely increased σ without significantly lowering the absolute S is crucial for the enhancement of the electrical power factor (PF, $PF = S^2\sigma$) in a TE material³.

Electronic band engineering has been the leading strategy that enhances the PF of TE materials. The milestone work by Hicks and Dresselhaus proposed that the enhancement of TE performance is possible if the electrons are confined in one or two dimensions, corresponding to an abrupt change of the electronic density of states (DOS) at some energy levels^{4,5}, as schematically shown in Fig. 1a. This low-dimensionality strategy sparked the studies of TE materials with nanostructures, such as quantum-well superlattice structures⁴, nanowires⁶. However, owing to the difficulty in large-scale synthesis and measurements of superlattice structures and nanowires, more attention, later on, has

been shifted to the nanostructured bulk materials with the band engineering strategy as a powerful tool to tune the PF.

In 2008, an enhanced zT of above 1.5 at 773 K in the thallium-doped PbTe was reported by Heremans et al.⁷ by distorting the DOS. As illustrated in Fig. 1b, the resonant TI-impurity level locates in the electronic band and leads to the increased DOS. Apart from distorting the DOS with the resonant level, converging the electronic bands to achieve high valley degeneracy N_v was also demonstrated as a general strategy to boost the TE performance of bulk materials, such as PbTe_{1-x}Se_x⁸ and Mg₂Si_{1-x}Sn_x⁹. The DOS effective mass m_d^* is related to the valley degeneracy N_v and single-band effective mass m_b^* through the expression¹⁰: $m_d^* = N_v^{2/3}m_b^*$. As shown in Fig. 1c, when more bands converge to the E_F , a larger m_d^* is produced due to the increased N_v , contributing to a higher DOS and S without significantly reducing the carrier mobility μ if intervalley scattering is not serious¹¹. From the view of band structure engineering, both resonant level and band convergence strategies target the enhanced DOS near E_F , leading to the improvement of S , similar to the low-dimensionality strategy.

Besides the DOS, the curvature of an electronic band, which is inversely proportional to m_b^* , is another important feature of the electronic structure that can be engineered to modulate μ . A light band could guarantee a higher μ compared with the heavy one (Fig. 1d). In heavy-band TE materials, such as half-Heusler compound V_{1-x}Nb_xFeSb, the m_b^* can be reduced by increasing Nb content, which is beneficial for a higher μ without significantly

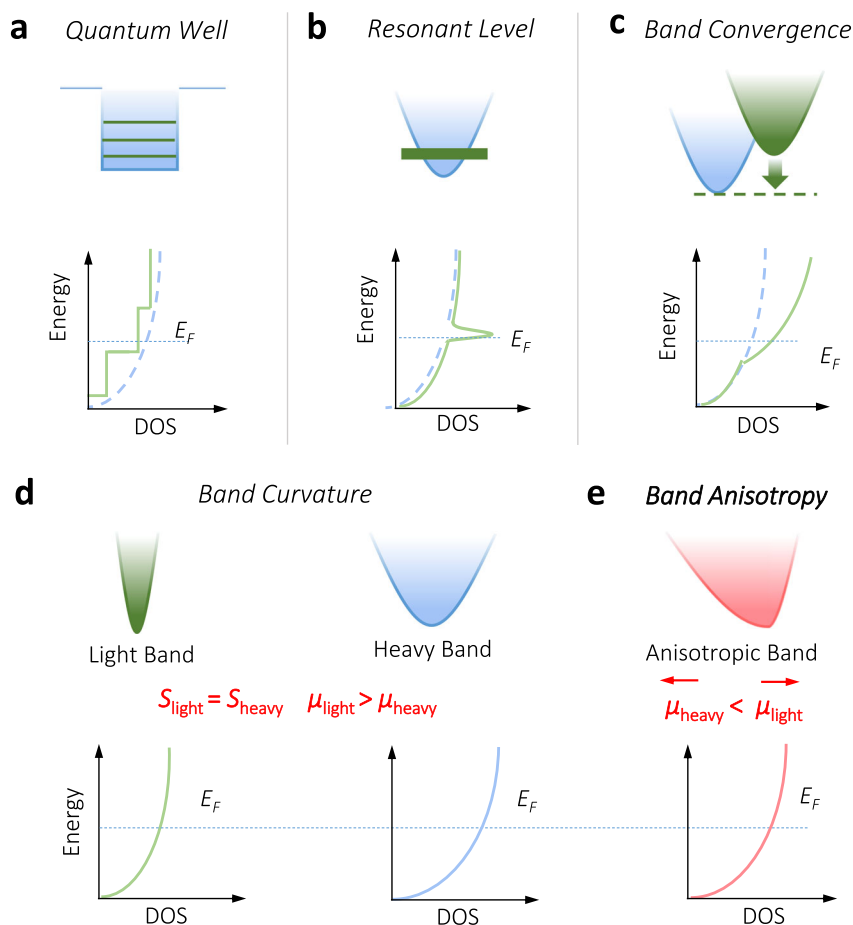


Fig. 1 Schematic representations of the band structures and DOS for different band engineering strategies. **a** Quantum well. **b** Resonant level. **c** Band convergence. **d** Band curvature and **e** band anisotropy. In **d** and **e**, the position E_F is assumed to be the same for the light band, heavy band, and anisotropic band, indicating the same S . The difference in the μ of light- and heavy-bands and along different directions of the anisotropic band is indicated.

lowering S , leading to an improved PF^{12,13}. The anisotropy of the electronic band along different directions is another important feature of the electronic structure in solids. Here, a band with very large anisotropy refers to a weak dispersion in one direction but a strong dispersion along the orthogonal direction^{14–16} (Fig. 1e). The valley anisotropy can be gauged by the anisotropy factor, $K = m_{\parallel}^*/m_{\perp}^*$, where m_{\parallel}^* and m_{\perp}^* is the band effective mass along with the parallel and perpendicular directions, respectively. Combined with N_v , the Fermi surface complexity factor has been recently proposed as an indicator in the high-throughput search of promising TE materials¹⁷. The important role of valley anisotropy in enhancing the TE performance has been highlighted from the view of theoretical calculations^{3,17}. However, the experimental route to utilize valley anisotropy to enhance the TE performance remains elusive.

For most heavily doped TE materials, the electronic transport properties could be understood using the single parabolic band (SPB) model (Supplementary Note 1)¹⁸. Assuming the carrier transport is the acoustic phonon scattering dominated, S can be expressed as

$$S = k_B/e[2F_1(\eta)/F_0(\eta) - \eta], \quad (1)$$

where k_B is the Boltzmann constant, e is the elemental charge, $F_i(\eta)$ is the Fermi integral, $\eta = E_F/k_B T$ is the reduced Fermi level. This expression indicates that S is only determined by η (the position of E_F), no matter the band is light or heavy (Fig. 1d). Bearing this in mind, one can deduce that for an anisotropic band the carrier transport along the light-band direction will show a higher μ while remaining the same S compared to the heavy-band direction. This suggests a feasible strategy to utilize the valley anisotropy to enhance the TE properties, specifically the PF.

Here, we experimentally demonstrate the effectiveness of utilizing valley anisotropy to enhance the TE performance by taking *p*-type Zintl phase compound Mg_3Sb_2 as a paradigm, which has a single anisotropic hole pocket at the center of the Brillouin zone (BZ). Based on the as-grown single crystals and textured polycrystalline samples, various methods were used to reveal the effect of valley anisotropy on the TE transport. An enhanced room-temperature zT by a factor of 3.6 was found if the carriers in *p*-type Mg_3Sb_2 transport along the light-band direction, compared to the heavy-band direction. Furthermore, given the p_z orbital overlapping as the indicator of valley anisotropy, the electronic structures of 66 isostructural Zintl phase compounds were calculated and 9 of them were screened out as promising candidates with potentially higher TE performance along the light-band direction.

Results

Valence band anisotropy in Mg_3Sb_2 . Experimentally, to demonstrate how valley anisotropy affects TE transport properties, it is paramount to select a suitable material system for carrying out the research. To minimize the effect of multiple pockets and the intervalley scattering, a material with a single Fermi pocket is preferable. To facilitate the analysis of the relation between the valley direction in the reciprocal space and the crystallographic direction in the real space, an anisotropic Fermi pocket locates at the center of the BZ is desirable. Moreover, the growth of single crystals should be feasible to enable the study of the anisotropic transport properties. With these criteria, *p*-type Mg_3Sb_2 single crystal¹⁹, which has a single anisotropic hole pocket locating at the center of the BZ, was selected for this study.

The Zintl phase compounds $\text{Mg}_3\text{Sb}_{2-x}\text{Bi}_x$ have recently attracted considerable attention due to the high *n*-type TE performance^{20–28}. Both Mg_3Sb_2 and Mg_3Bi_2 crystallize in a trigonal layered structure with the space group $P\bar{3}m1$, as shown in

Fig. 2a. Previous experimental studies²⁹ and calculations³⁰ suggest that the electron (*n*-type) transport of $\text{Mg}_3\text{Sb}_{2-x}\text{Bi}_x$ exhibit a very weak anisotropy, owing to the six nearly spherical electron pockets. In contrast, there is only one-hole pocket in the center of the BZ for Mg_3Sb_2 if the hole carrier density n is below 10^{20} cm^{-3} (Fig. 2b). The plate-like Fermi surface suggests that the hole carrier transport in the k_x – k_y plane is nearly isotropic but becomes quite different along the k_z direction, corresponding to the ab-plane and *c*-axis in the real space, respectively.

The anisotropy of Mg_3Sb_2 is more clearly presented in the calculated valence band structure (Fig. 2c), i.e., a large difference in the curvature along with Γ –K and Γ –A directions, which can be quantified by the effective mass: it is $0.9m_e$ along Γ –K direction while $0.11m_e$ along Γ –A direction. A K value of about 8.2 is thus derived. This result is close to the calculations by Zhang et al.³¹ ($m_{\Gamma\text{-K}}^* = 1.15m_e$, $m_{\Gamma\text{-A}}^* = 0.15m_e$) and Meng et al.³⁰ ($m_{\Gamma\text{-K}}^* = 0.61m_e$, $m_{\Gamma\text{-A}}^* = 0.07m_e$), giving the K values of 7.7 and 8.7, respectively. To confirm the valence band anisotropy, we further performed angle-resolved photoemission spectroscopy (ARPES) study to reveal the experimental valence band structure of Mg_3Sb_2 . As shown in Fig. 2d, the band curvature along Γ –K and Γ –M directions are identical, suggesting an isotropic transport along the ab-plane. In contrast, a significant steep band structure is observed along the Γ –A direction. Based on the ARPES results, the $m_{\Gamma\text{-K}}^*$ and $m_{\Gamma\text{-A}}^*$ are estimated to be $0.9m_e$ and $0.16m_e$, respectively, giving a K value of about 5.6, which is close to the calculated values ($K \sim 8$). Thus, the single anisotropic valence band of Mg_3Sb_2 makes it an ideal system to demonstrate the effect of valley anisotropy on the TE properties.

***P*-type Mg_3Sb_2 single crystals.** To study the effect of valley anisotropy on TE transport, high-quality single crystals with a sizable dimension are required. Previously, Mg_3Sb_2 single crystals were successfully grown using the flux method^{19,26,27}, which exhibits a thin-layered shape with a typical thickness smaller than 1 mm. Such a small thickness makes it difficult to study the TE transport properties along the *c*-axis. Here, the single crystals of Ag-doped Mg_3Sb_2 were prepared through the slow-cooling method. Silver was previously found to be a good acceptor³² and thus used to shift the E_F into the valence band. As shown in the inset of Fig. 3a and Supplementary Fig. 1a, the as-grown crystal shows clear cleavage surfaces, of which the crystallinity and orientation were checked using the XRD and Laue diffraction (Supplementary Fig. 1). The EDS mapping and line scanning were carried out to check the chemical homogeneity (Supplementary Fig. 2). The results indicate that the chemical composition is homogeneous. Bar-shaped crystals with the size of about $1 \times 1 \times 3 \text{ mm}^3$ were cut for electrical and thermal transport measurements in the temperature range of 100–300 K.

The Hall carrier mobility μ_H of the crystals is shown in Fig. 3a. Along the *c*-axis, the μ_H is about 300% of that along the ab-plane in the whole temperature range, as expected from the anisotropic valence band (Fig. 2), which is in agreement with our previous study on the isostructural *p*-type Mg_3Bi_2 single-crystal reporting that σ along the *c*-axis is 200% higher than that along the ab-plane¹⁹. These results suggest that the carrier transport along the light-band direction is faster than that along the heavy-band direction, probably owing to the weaker carrier scattering and low inertial effective mass. The S and the Hall carrier density n_H along both directions are shown in Fig. 3b. Very interestingly, distinct from the huge difference in the μ_H , the S values along both directions are close to each other, given the measurement uncertainty. These results suggest a much higher PF when the hole carriers in Mg_3Sb_2 move along the *c*-axis.

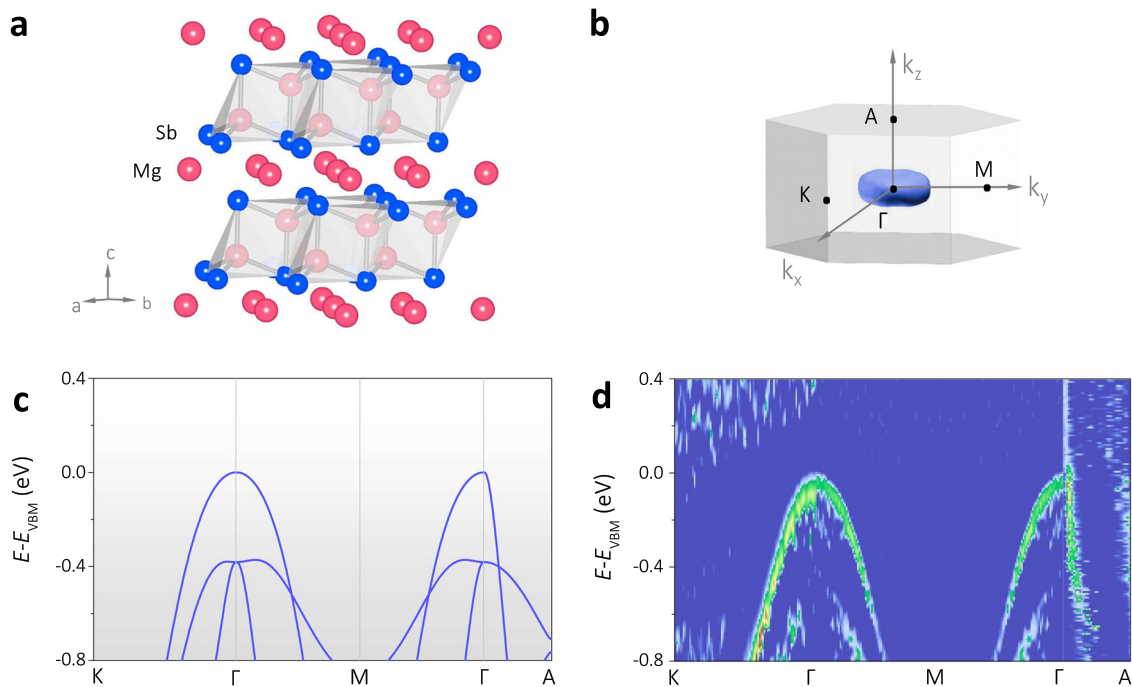


Fig. 2 The crystal and band structures of Mg_3Sb_2 . **a** Crystal structure. **b** Calculated Fermi surface at a hole concentration of $\sim 10^{20} \text{ cm}^{-3}$, and **c** the calculated valence band structure for Mg_3Sb_2 . **d** ARPES results of the valence band structure of Mg_3Sb_2 , Γ –K and Γ –M show nearly the same curvature, while Γ –M and Γ –A show a distinct anisotropy, which corresponds to the plate-like Fermi surface presented in **b**.

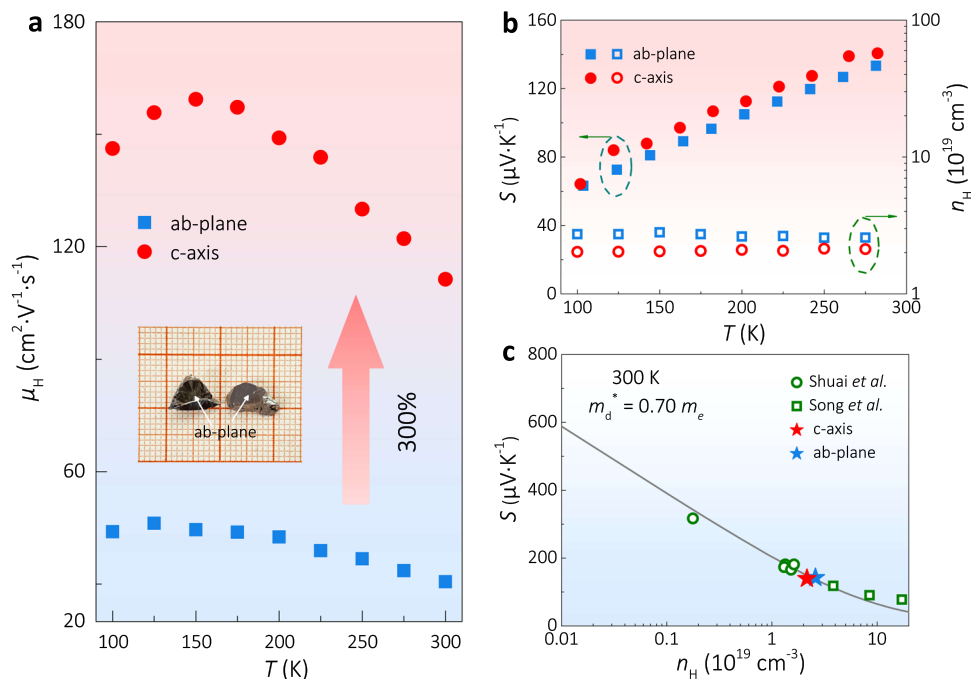


Fig. 3 The electrical properties of single crystal Mg_3Sb_2 . Temperature dependences of **a** μ_H , and **b** S and n_H for the Ag-doped Mg_3Sb_2 single crystal along c-axis and ab-plane. **c** Pisarenko plot showing the relationship between S and n_H . The curve was calculated using the SPB model¹⁸ with the m_d^* of $0.70m_e$. The experimental data of the single crystals in this work and polycrystalline samples^{32,33} are displayed. The inset in **a** is the optical image of the as-grown single crystals with a clear cleavage plane.

For p-type Mg_3Sb_2 , even though the effective masses along ab-plane and c-axis directions are different, the S should in principle be similar due to the unchanged Fermi level, as expected from Eq. (1). The relationship among S , m_d^* , and n_H could be presented by the so-called Pisarenko plot. As shown in Fig. 3c, the experimental data of the single crystals along both directions

agree well with the calculated line and also the data for polycrystalline samples^{32,33}. This further confirms that S is not orientation-dependent in p-type Mg_3Sb_2 . The almost unchanged S and n_H but largely distinct μ along different directions demonstrate that the valley anisotropy is an effective means to decouple the S and σ to realize a better PF in p-type Mg_3Sb_2 .

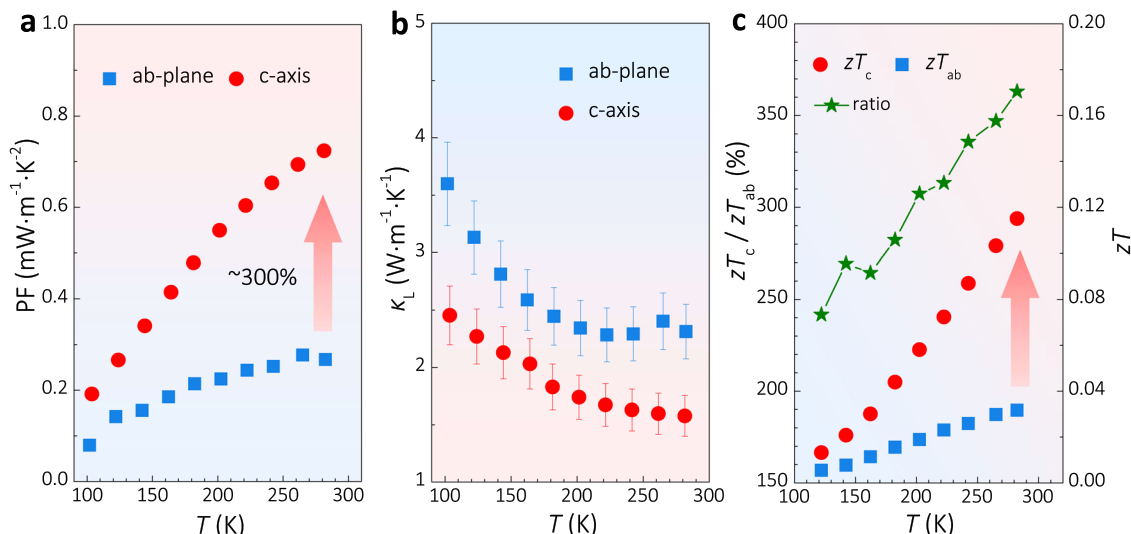


Fig. 4 The TE properties of single-crystal Mg_3Sb_2 . Temperature dependences of **a** PF; **b** κ_L ; **c** zT ; and zT ratio along c-axis and ab-plane for the Ag-doped Mg_3Sb_2 single crystal.

Because of the almost similar S but much larger σ , the PF along the c -axis is nearly 300% of that along the ab-plane, as shown in Fig. 4a. We further measured the κ along both directions using a four-probe steady-state method (schematically shown in Supplementary Fig. 3). The κ_L was obtained by subtracting the electronic part of thermal conductivity according to the Wiedemann–Franz law. The results (Fig. 4b) imply a slight anisotropy in the κ_L of Mg_3Sb_2 , in which the κ_L along c -axis is $1.6 \text{ W m}^{-1} \text{ K}^{-1}$ at 300 K, which is about 30% lower than that in ab-plane ($2.3 \text{ W m}^{-1} \text{ K}^{-1}$ at 300 K). The slight upturn of κ_L above 200 K might come from the heat radiation effect. Previously, Zhang et al.³⁴ argued that the κ_L is nearly isotropic ($\kappa_a/\kappa_c \approx 1.1$ at 300 K) in Mg_3Sb_2 based on analyzing the chemical bonding in both intra-layer and inter-layer. Later on, the calculations using the finite temperature method by Zhu et al.³⁵ showed that there is an anisotropy in the κ_L of Mg_3Sb_2 . That is, the κ_L along the c -axis is about 20% lower than that in the ab-plane. Together with current experimental results, we could conclude that the κ_L of Mg_3Sb_2 along the c -axis is lower than that along the ab-plane, albeit slightly. One of the reasons leading to the anisotropy in κ_L is that the average group velocities in the c -axis are smaller than the ab-plane, according to the calculations by Zhu et al.³⁵. Besides, MgI–Sb chemical bonding in the interlayer of Mg_3Sb_2 is weaker³⁴, which could be another factor leading to the anisotropy in κ_L .

Due to the much higher PF and smaller κ_L , Mg_3Sb_2 single crystal exhibits a larger zT when the carrier transport along the c -axis (Fig. 4c). Specifically, near 300 K, the zT along the c -axis is about 260% higher than that along the ab-plane. This result demonstrates a feasible strategy to realize a better TE performance by utilizing valley anisotropy.

Textured polycrystalline Mg_3Sb_2 . Owing to the relatively small size of the as-grown Mg_3Sb_2 single crystal, the measurements of TE properties above room temperature are difficult using commercial equipment which usually requires samples in a centimeter size. Thus, to study the effect of valley anisotropy on high-temperature transport properties of Mg_3Sb_2 , we further prepared the textured polycrystalline samples with suitable sizes (details shown in the method section), facilitating the measurements above room temperature. Figure 5a and Supplementary Fig. 4 show the XRD patterns of the textured polycrystalline samples along parallel ($//P$) and vertical ($\perp P$) to the pressing direction. The intensity ratio I_{002}/I_{110} of $\perp P$ is 1.56, much stronger than that

of $//P$ (1.05), indicating that the grains in the polycrystalline samples are textured. Moreover, the scanning electron microscopy (SEM) images of both $//P$ and $\perp P$ are displayed in Supplementary Fig. 5, further verifying the textured structures.

Even if the samples are textured, similar S along different directions is still observed (Fig. 5b). More importantly, the higher σ of $//P$ is higher (Fig. 5c), as expected from the single-crystal study (Fig. 3). Meanwhile, the κ_L of the textured Mg_3Sb_2 polycrystalline samples also shows a slight anisotropic character (Fig. 5d), although it is weaker compared to that in the single crystal (Fig. 4b). Hence, the PF and zT for the sample $//P$ are much higher than that of $\perp P$ (Fig. 5e). Moreover, it is worth noting that the zT of $//P$ is improved in the whole temperature range. This indicates a higher device ZT^{36} for the sample $//P$, which is about 60% higher than that of $\perp P$ (inset of Fig. 5e). As a supplemental confirmation, we also found a higher TE performance along with $//P$ in other $\text{Mg}_{3-x}\text{Ag}_x\text{Sb}_{2-y}\text{Bi}_y$ samples, despite having different contents of Bi and Ag (Supplementary Figs. 6–9). The results from the textured polycrystalline samples, as well as the single crystals, demonstrate the effectiveness of utilizing valley anisotropy to enhance the TE performance.

Furthermore, it is meaningful to make a comparison of the anisotropic transport properties of the studied Mg_3Sb_2 with the other “layer-structured” TE materials, such as Bi_2Te_3 , SnSe , and SnSe_2 . Although all of them show anisotropic TE properties, the observed highest zT occurs in different crystallographic directions, either the in-plane or the cross-plane direction. Both n-type and p-type Bi_2Te_3 -based materials exhibit higher zT along the in-plane direction, owing to the higher μ ³⁷, despite also having a higher κ_L in the same direction. The n-type SnSe ³⁸ and SnSe_2 ³⁹ show a higher zT along the cross-plane direction, mainly contributed by the much lower κ_L . In contrast, p-type Mg_3Sb_2 is an exceptional case because that it shows not only a lower κ_L but also a much higher μ in the cross-plane direction. It might be common for the “layer-structured” materials to show a lower κ_L along the cross-plane direction but is rather rare to exhibit a much higher μ . Therefore, a further understanding of the origin of the valley anisotropy in p-type Mg_3Sb_2 is important.

Valley anisotropy in AB_2X_2 Zintl phase compounds. The calculations of the orbital-projected band structures were performed and the enlarged details of the valence band maximum (VBM) for Mg_3Sb_2 are displayed in Fig. 6a. It is found that the p_z orbital of

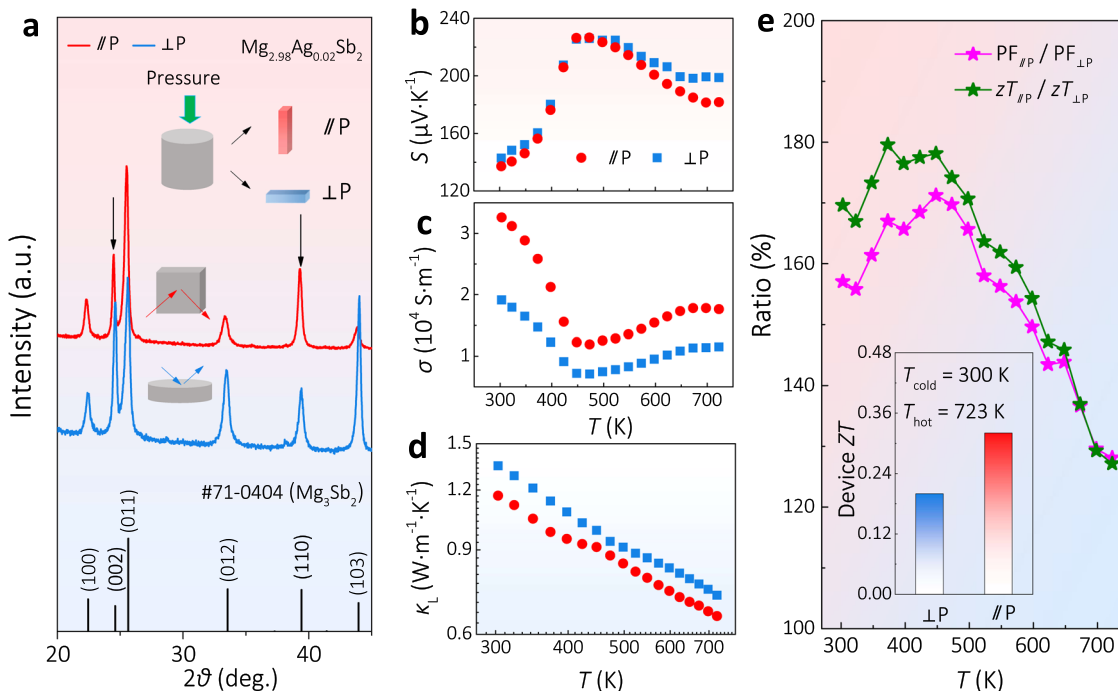


Fig. 5 The structure and TE properties of textured polycrystalline Mg_3Sb_2 . **a** XRD patterns, temperature dependences of **b** S , **c** σ , **d** κ_L , **e** zT , and PF ratios for the textured polycrystalline Mg_3Sb_2 samples. The inset in **e** shows the calculated device ZT^{36} .

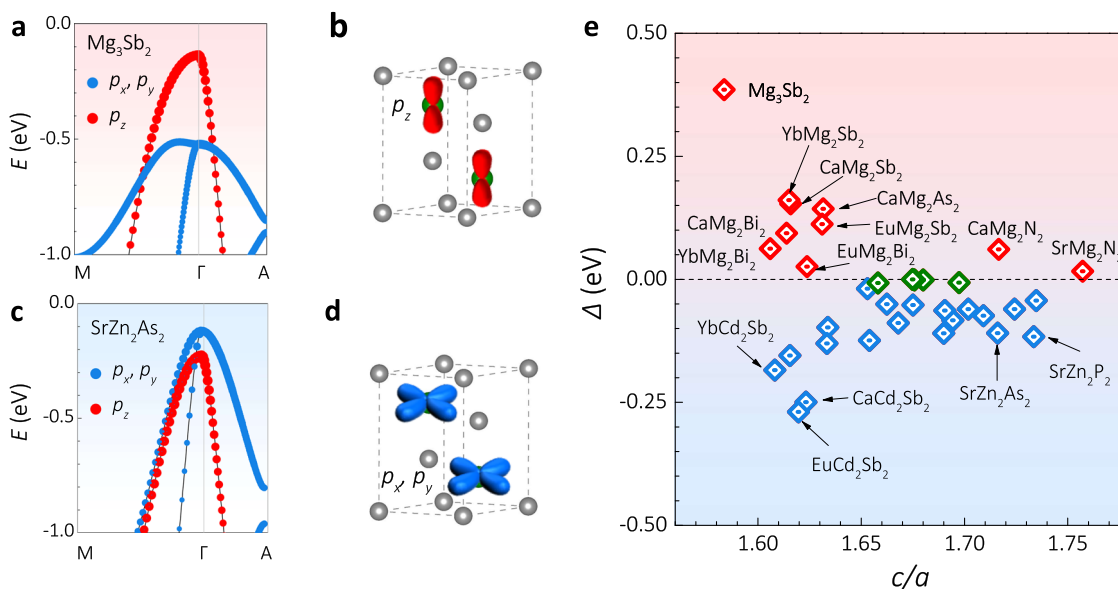


Fig. 6 The band structure of AB_2X_2 Zintl phase compounds. **a** Orbital projected band structures of Mg_3Sb_2 . **b** Schematic diagram of the p_z orbital-dominated hole transport in Mg_3Sb_2 . **c** Orbital projected band structures of SrZn_2As_2 . **d** Schematic diagram about (p_x, p_y) orbitals-dominated hole transport in SrZn_2As_2 . **e** Crystal field splitting energy versus lattice ratio c/a for AB_2X_2 Zintl phase system.

Sb dominates the VBM (red dots) at the Γ point. In real space, the dumbbell-shaped p_z orbital corresponds to the anisotropy of the valence band (Fig. 6b). More specifically, p_z orbital will be more overlapping along the c -axis than in the ab -plane, indicating that the valence band is much dispersive along the c -axis. The p_z -orbital dominated VBM phenomenon is a result of the crystal field splitting effect^{40,41}. Mg_3Sb_2 belongs to the AB_2X_2 Zintl phase compounds family (A is alkaline earth or lanthanides element, B is Mg or VIIB or IIB or IIIA group element, X is IVA or VA group element)⁴², it is thus interesting to investigate whether other candidates from this family show a similar anisotropic

VBM. Owing to the effect of crystal field splitting, the position of p_z orbital could be either above ($\Delta > 0$) or below ($\Delta < 0$) the (p_x, p_y) orbitals depending on the value of crystal field splitting energy Δ [$\Delta = E(p_z) - E(p_x, p_y)$]. The (p_x, p_y) orbitals-dominated VBM (blue dots in Fig. 6c) is observed in another Zintl compound SrZn_2As_2 . Different from Mg_3Sb_2 , more overlapping of (p_x, p_y) orbitals are expected in ab -plane (Fig. 6d) in real space, which implies higher hole mobility in the ab -plane for SrZn_2As_2 .

The AB_2X_2 Zintl phase compounds are a big family which shows great potential to be explored as the TE candidates^{43,44}. According to the Zintl chemistry, smaller κ_L along the c -axis is

expected for all the AB_2X_2 compounds due to the ionic bonding between the interlayers^{34,45}. If these compounds possess a similar anisotropic valence band structure to that of Mg_3Sb_2 , it will promise higher TE performance when the carriers transport along the c -axis. To search for other potential candidates, the first-principles calculations were further conducted to investigate the band structure of 66 AB_2X_2 Zintl compounds (Supplementary Figs. 10–23, Supplementary Table 1). Out of them, we found 9 candidates (Fig. S9) that have a similar valence band anisotropy as Mg_3Sb_2 . Moreover, the anisotropic factor K was also estimated for the 9 candidates (Supplementary Table 2) and some of them are even larger than that of Mg_3Sb_2 , indicating that they will also exhibit good TE performance along the c -axis. For example, $CaMg_2Bi_2$ is one of the 9 candidates. Previously, the $CaMg_2Bi_2$ polycrystalline sample, without considering the anisotropy, was found to be a good p-type TE material with a peak zT of about 1.3 at 873 K⁴⁶. According to our calculations, $CaMg_2Bi_2$ exhibits a strong valence band anisotropy ($K \sim 16$). Hence, if the single crystals or textured polycrystalline samples of $CaMg_2Bi_2$ can be made, one can expect even higher zT along the c -axis owing to the higher μ and lower κ_L .

We also notice that some other AB_2X_2 compounds have a similar band structure as that of $SrZn_2As_2$ (Supplementary Figs. 13–16), indicating a higher μ along the ab -plane. The anisotropic TE performance of these AB_2X_2 compounds with (p_x, p_y)-orbitals-dominated VBM is thus determined by the trade-off between μ and κ_L along the c -axis and ab -plane. It is worth noting that the crystal field splitting energy Δ of some AB_2X_2 compounds is nearly zero (green dots in Fig. 6e), indicating a high orbital band degeneracy. Under this condition, the anisotropy of VBM is not obvious, but the high orbital band degeneracy might benefit the improved TE performance, as previously argued by Zhang et al.^{41,47} Thus, both band anisotropy and orbital degeneracy play significant roles in obtaining high TE performance in the light of their valence band structure. Different band engineering strategies, either band anisotropy or band convergence, can thus be considered to enhance their TE performance. Beyond AB_2X_2 Zintl phase compounds, recent years have witnessed the discoveries of many TE materials with non-cubic crystal structures. Hence the anisotropy in the electronic valley and phonon dispersion offers an additional degree of freedom that can be utilized to enhance TE performance.

Discussion

From the above experiments on p-type Mg_3Sb_2 , the facts why valley anisotropy can be utilized to realize the enhanced TE performance are summarized: one is the higher μ in the light-band direction, the other is the almost unchanged S and n in both light-band and heavy-band directions. These results suggest that the μ is more sensitive to the band curvature while S and n are not⁴⁸. The anisotropic factor K for p-type Mg_3Sb_2 is about 5.6, which is similar to other good TE materials, such as $ZrNiSn$ ($K \sim 8$)⁴⁹, Bi_2Te_3 ($K \sim 2.6$)⁵⁰. This indicates the generality of utilizing valley anisotropy to realize the enhanced PF in conventional TE materials. In some other cases, such as the layered metal NaN_2As_2 ⁵¹, the electronic structure shows multiple electron and hole pockets near the Fermi level. As a result, the S of NaN_2As_2 exhibits opposite signs along with different crystallographic directions, owing to the significant change in the Fermi surface curvature. Such cases are out of the scope of the current TE research focusing on semiconductors with a single type of carrier.

In summary, in our opinion, the S will not display an obvious difference along with different crystallographic directions for most semiconductors with valley anisotropy. However, μ is very sensitive to the curvature of the electronic valley, which offers an

opportunity to realize higher μ while keeping S unchanged. This is different from the previous band engineering strategies, such as band convergence and resonant states, which focus on the enhancement of the S by regulating the DOS. Taking p-type Mg_3Sb_2 as a model system, we demonstrate that valley anisotropy can be utilized as an effective means to decouple the correlation between S and μ , leading to the realization of enhanced power factor. Compared to the heavy-band direction, the carriers show much higher μ while the S keeps unchanged if they transport along the light-band direction, resulting in an increased power factor by a factor of 3. This conclusion is also suitable to other isostructural AB_2X_2 Zintl phase compounds with p_z orbital-dominated valence band, which usually have a lower κ_L along the light-band direction as well. Moreover, utilizing valley anisotropy can also be a feasible strategy to enhance the performance of other TE materials with anisotropic electronic structures.

Methods

Sample preparation. For synthesizing the single-crystal samples, starting elements Mg (granules, 99.8%), Sb (shot, 99.999%), and Ag (shot, 99.999%) were weighted and mixed with a molar ratio of Mg:Sb:Ag = 2.98:2:0.02. The tantalum tubes with an inner diameter of 10 mm were used to store the mixtures and then sealed under argon atmosphere using an arc melter. Afterward, these tantalum tubes were put into the sealed quartz tubes and heated up to 1453 K, and dwelled for 24 h ensuring homogeneity. For crystal growth, the tubes were slowly cooled down to 923 K with a cooling rate of 2.5 K/h. For preparing the polycrystalline samples $Mg_{3-x}Ag_xSb_2$ and $Mg_{3-x}Ag_xSb_{1.5}Bi_{0.5}$ ($x = 0.015, 0.02, 0.025$), starting elements Mg (granules, 99.8%), Sb (shot, 99.999%), Bi (shot, 99.999%), and Ag (shot, 99.999%) were weighed and mixed nominally and then were melted in Ta tube as the same procedure as described for single crystals. The obtained ingots (≈ 12 g) were loaded into graphite dies (diameter: 12.7 mm) for spark plasma sintering process (SPS) (SPS-1050; Sumitomo Coal Mining Co.) under 923 K and 60 MPa in a vacuum for 10 min. For structural characterization and transport measurements, the obtained samples were cut along the directions that are parallel and perpendicular to the pressing direction, respectively, as shown in the inset of Fig. 5a.

Characterization. The single crystals were checked and oriented at room temperature by the white-beam backscattering Laue X-ray diffraction (XRD) method (Rigaku AFC7 plus Saturn 724 + CCD). For the polycrystalline samples, the XRD (Rigaku, Rint 2000, CuK_α) and SEM (Hitachi, S-3400N, 15 kV) analyses were performed along parallel ($//P$) and vertical ($\perp P$) to the pressing direction to characterize the texture. To experimentally reveal the valence band structure, we carried out the angle-resolved photoemission spectroscopy (ARPES) measurements of Mg_3Sb_2 single crystals at the UE112-PGM2b beamline of the synchrotron radiation facility BESSY (Berlin) with 1^3 and 1^2 end stations, equipped with DA30L and R800 analyzers, respectively. The total energy resolution is about 15 meV while the angular resolution is 0.2° . The crystals were cleaved in situ and measured at 20 K.

Measurements. Single crystals with dimensions of about $1 \times 1 \times 3$ mm³ were employed for the transport measurements. The resistivity (ρ) and Hall resistivity (ρ_H) were measured simultaneously using a PPMS-9T instrument (Quantum Design) using the ACT option via a standard four-probe method. Hall carrier density n_H and mobility μ_H are obtained from $n_H = 1/eR_H$, and $\mu_H = R_H/\rho$, where R_H is the Hall coefficient. TE transport properties were measured with a steady-state heat sink method in the high vacuum condition with a breakout box⁵¹. A strain gauge heater was placed on one end of the sample to apply the heat power. Two type-E thermocouples were attached along with the sample for measuring the temperature difference, with the chromel leg used for thermopower measurement. The thermal conductivity κ was then calculated by the formula $\kappa = W/(\Delta T dw)$, where W is the applied heater power, ΔT is the temperature difference, l , d , and w is the length between the two thermocouples, width, and thickness of the sample, respectively. For measuring the S , we applied various heater currents at selected temperatures and measured the TE voltage as a function of temperature difference. The slope of ΔV over ΔT is taken as the relative Seebeck with respect to the chromel. For the polycrystalline sample, the commercial Linseis LSR-3 system was used for the measurements of the Seebeck coefficient S and the electrical conductivity σ from 300 to 700 K with an accuracy of about $\pm 5\%$ and $\pm 3\%$, respectively. Netzsch LFA457 was used for the measurement of the thermal diffusivity D with an accuracy of about $\pm 3\%$. The thermal conductivity κ was calculated from the equation: $\kappa = D\rho C_p$. The sample density ρ was estimated by the Archimedes method and the heat capacity C_p was calculated by the method proposed by Agne et al.⁵²: $C_p = 3NR/M_w \times (1 + 1.3 \times 10^{-4}T - 4 \times 10^{-3}T^2)$, where N is the number of elements in the formula unit, R is the gas constant, M_w is the molecular weight of the formula unit.

Band structure calculations. The density functional theory was employed in this work using the Vienna ab initio Simulation Package^{53,54} with the projector augmented-wave method⁵⁵. Perdew–Burke–Ernzerhof type generalized gradient approximation was used as the exchange–correlation functional⁵⁶. A plane-wave energy cutoff of 400 eV and an energy convergence criterion of 10^{-5} eV for self-consistency was adopted. All the atomic positions were relaxed to equilibrium until the calculated Hellmann–Feynman force on each atom was <0.01 eV/Å. The Monkhorst–Pack uniform k -point sampling with $k = 60/L$ (L is the corresponding lattice parameter) was used in self-consistent static calculations for charge density and dielectric constant. Non-self-consistent calculations were then performed to calculate the band structures using the converged charge density and a Gaussian broadening of 0.05 eV was used.

Reporting summary. Further information on experimental design is available in the Nature Research Reporting Summary linked to this paper.

Data availability

The experiment data that support the findings of this study are available from the corresponding author upon reasonable request.

Received: 14 June 2021; Accepted: 26 August 2021;

Published online: 17 September 2021

References

- He, J. & Tritt, T. M. Advances in thermoelectric materials research: looking back and moving forward. *Science* **357**, eaak9997 (2017).
- Snyder, G. J. & Toberer, E. S. Complex thermoelectric materials. *Nat. Mater.* **7**, 105–114 (2008).
- Zhu, T. et al. Compromise and synergy in high-efficiency thermoelectric materials. *Adv. Mater.* **29**, 1605884 (2017).
- Hicks, L. D., Harman, T. C., Sun, X. & Dresselhaus, M. S. Experimental study of the effect of quantum-well structures on the thermoelectric figure of merit. *Phys. Rev. B* **53**, R10493–R10496 (1996).
- Dresselhaus, M. S. et al. New directions for low-dimensional thermoelectric materials. *Adv. Mater.* **19**, 1043–1053 (2007).
- Heremans, J. P., Thrush, C. M., Morelli, D. T. & Wu, M.-C. Thermoelectric power of bismuth nanocomposites. *Phys. Rev. Lett.* **88**, 216801 (2002).
- Heremans, J. P. et al. Enhancement of thermoelectric efficiency in PbTe by distortion of the electronic density of states. *Science* **321**, 554 (2008).
- Pei, Y. et al. Convergence of electronic bands for high performance bulk thermoelectrics. *Nature* **473**, 66–69 (2011).
- Liu, W. et al. Convergence of conduction bands as a means of enhancing thermoelectric performance of n -type $\text{Mg}_2\text{Si}_{1-x}\text{Sn}_x$ solid solutions. *Phys. Rev. Lett.* **108**, 166601 (2012).
- Goldsmid, H. J. *Introduction to Thermoelectricity*, Vol. 121 (Springer, 2016).
- Norouzzadeh, P. & Vashaee, D. Classification of valleytronics in thermoelectricity. *Sci. Rep.* **6**, 22724 (2016).
- Fu, C., Zhu, T., Liu, Y., Xie, H. & Zhao, X. Band engineering of high performance p -type FeNbSb based half-Heusler thermoelectric materials for figure of merit $zT > 1$. *Energy Environ. Sci.* **8**, 216–220 (2015).
- Fu, C. et al. Realizing high figure of merit in heavy-band p -type half-Heusler thermoelectric materials. *Nat. Commun.* **6**, 8144 (2015).
- Parker, D., Chen, X. & Singh, D. J. High three-dimensional thermoelectric performance from low-dimensional bands. *Phys. Rev. Lett.* **110**, 146601 (2013).
- Parker, D. S., May, A. F. & Singh, D. J. Benefits of carrier-pocket anisotropy to thermoelectric performance: the case of p -type AgBiSe_2 . *Phys. Rev. Appl.* **3**, 064003 (2015).
- Bilc, D. I., Hautier, G., Waroquiers, D., Rignanese, G.-M. & Ghosez, P. Low-dimensional transport and large thermoelectric power factors in bulk semiconductors by band engineering of highly directional electronic states. *Phys. Rev. Lett.* **114**, 136601 (2015).
- Gibbs, Z. M. et al. Effective mass and Fermi surface complexity factor from ab initio band structure calculations. *npj Comput. Mater.* **3**, 8 (2017).
- May, A. F. & Snyder, G. J. In *Materials, Preparation, and Characterization in Thermoelectrics* (CRC Press, 2017).
- Xin, J. et al. Growth and transport properties of Mg_3X_2 ($X = \text{Sb}, \text{Bi}$) single crystals. *Mater. Today Phys.* **7**, 61–68 (2018).
- Tamaki, H., Sato, H. K. & Kanno, T. Isotropic conduction network and defect chemistry in $\text{Mg}_{3+\delta}\text{Sb}_2$ -based layered zintl compounds with high thermoelectric performance. *Adv. Mater.* **28**, 10182–10187 (2016).
- Zhang, J. et al. Discovery of high-performance low-cost n -type Mg_3Sb_2 -based thermoelectric materials with multi-valley conduction bands. *Nat. Commun.* **8**, 13901 (2017).
- Shi, X. et al. Extraordinary n -Type Mg_3SbBi thermoelectrics enabled by yttrium doping. *Adv. Mater.* **31**, 1903387 (2019).
- Mao, J. et al. High thermoelectric cooling performance of n -type Mg_3Bi_2 -based materials. *Science* **365**, 495 (2019).
- Shu, R. et al. $\text{Mg}_{3+\delta}\text{Sb}_2\text{Bi}_{2-x}$ family: a promising substitute for the state-of-the-art n -type thermoelectric materials near room temperature. *Adv. Funct. Mater.* **0**, 1807235 (2018).
- Zhang, F. et al. High-performance N -type Mg_3Sb_2 towards thermoelectric application near room temperature. *Adv. Funct. Mater.* **30**, 1906143 (2019).
- Pan, Y. et al. $\text{Mg}_3(\text{Bi},\text{Sb})_2$ single crystals towards high thermoelectric performance. *Energy Environ. Sci.* **13**, 1717–1724 (2020).
- Imasato, K. et al. Metallic n -type Mg_3Sb_2 single crystals demonstrate the absence of ionized impurity scattering and enhanced thermoelectric performance. *Adv. Mater.* **32**, e1908218 (2020).
- Imasato, K., Kang, S. D. & Snyder, G. J. Exceptional thermoelectric performance in $\text{Mg}_3\text{Sb}_{0.6}\text{Bi}_{1.4}$ for low-grade waste heat recovery. *Energy Environ. Sci.* **12**, 965–971 (2019).
- Song, S. et al. Study on anisotropy of n -type Mg_3Sb_2 -based thermoelectric materials. *Appl. Phys. Lett.* **112**, 092103 (2018).
- Meng, F. et al. Anisotropic thermoelectric figure-of-merit in Mg_3Sb_2 . *Mater. Today Phys.* **13**, 100217 (2020).
- Zhang, J., Song, L. & Iversen, B. B. Insights into the design of thermoelectric Mg_3Sb_2 and its analogs by combining theory and experiment. *npj Comput. Mater.* **5**, 76 (2019).
- Song, L., Zhang, J. & Iversen, B. B. Simultaneous improvement of power factor and thermal conductivity via Ag doping in p -type Mg_3Sb_2 thermoelectric materials. *J. Mater. Chem. A* **5**, 4932–4939 (2017).
- Shuai, J. et al. Thermoelectric properties of Na-doped Zintl compound: $\text{Mg}_{3-x}\text{Na}_x\text{Sb}_2$. *Acta Mater.* **93**, 187–193 (2015).
- Zhang, J., Song, L., Sist, M., Tolborg, K. & Iversen, B. B. Chemical bonding origin of the unexpected isotropic physical properties in thermoelectric Mg_3Sb_2 and related materials. *Nat. Commun.* **9**, 4716 (2018).
- Zhu, Y. et al. Violation of the $T-1$ relationship in the lattice thermal conductivity of Mg_3Sb_2 with locally asymmetric vibrations. *Research* **2020**, 4589786 (2020).
- Snyder, G. J. & Snyder, A. H. Figure of merit ZT of a thermoelectric device defined from materials properties. *Energy Environ. Sci.* **10**, 2280–2283 (2017).
- Carle, M., Pierrat, P., Lahalle-Gravier, C., Scherrer, S. & Scherrer, H. Transport properties of n -type $\text{Bi}_2(\text{Te}_{1-x}\text{Se}_x)_3$ single crystal solid solutions ($x \leq 0.05$). *J. Phys. Chem. Solids* **56**, 201–209 (1995).
- Chang, C. et al. 3D charge and 2D phonon transports leading to high out-of-plane ZT in n -type SnSe crystals. *Science* **360**, 778 (2018).
- Xu, P. et al. Anisotropic thermoelectric properties of layered compound SnSe_2 . *Sci. Bull.* **62**, 1663–1668 (2017).
- Tan, X. et al. Band engineering and crystal field screening in thermoelectric Mg_3Sb_2 . *J. Mater. Chem. A* **7**, 8922–8928 (2019).
- Zhang, J. et al. Designing high-performance layered thermoelectric materials through orbital engineering. *Nat. Commun.* **7**, 10892 (2016).
- Kauzlarich, S. M., Zevalkink, A., Toberer, E. & Snyder, G. J. In *Thermoelectric Materials and Devices 1–26* (The Royal Society of Chemistry, 2017).
- Kauzlarich, S. M., Brown, S. R. & Jeffrey Snyder, G. Zintl phases for thermoelectric devices. *Dalton Trans.* **21**, 2099–2107 (2007).
- Toberer, E. S., May, A. F. & Snyder, G. J. Zintl chemistry for designing high efficiency thermoelectric materials. *Chem. Mater.* **22**, 624–634 (2010).
- Peng, W., Petretto, G., Rignanese, G.-M., Hautier, G. & Zevalkink, A. An unlikely route to low lattice thermal conductivity: small atoms in a simple layered structure. *Joule* **2**, 1879–1893 (2018).
- Shuai, J. et al. Higher thermoelectric performance of Zintl phases ($\text{Eu}_{0.5}\text{Yb}_{0.5}$) $_{1-x}\text{Ca}_x\text{Mg}_2\text{Bi}_2$ by band engineering and strain fluctuation. *Proc. Natl Acad. Sci. USA* **113**, E4125 (2016).
- Zhang, J. et al. High-performance pseudocubic thermoelectric materials from non-cubic chalcopyrite compounds. *Adv. Mater.* **26**, 3848–3853 (2014).
- Bies, W. E., Radtke, R. J., Ehrenreich, H. & Runge, E. Thermoelectric properties of anisotropic semiconductors. *Phys. Rev. B* **65**, 085208 (2002).
- Fu, C. et al. Revealing the intrinsic electronic structure of 3D half-Heusler thermoelectric materials by angle-resolved photoemission spectroscopy. *Adv. Sci.* **7**, 1902409 (2020).
- Stordeur, M., Stölzer, M., Sobotta, H. & Riede, V. Investigation of the valence band structure of thermoelectric $(\text{Bi}_{1-x}\text{Sb}_x)_2\text{Te}_3$ single crystals. *Phys. Status Solidi B* **150**, 165–176 (1988).
- He, B. et al. The Fermi surface geometrical origin of axis-dependent conduction polarity in layered materials. *Nat. Mater.* **18**, 568–572 (2019).
- Agne, M. T. et al. Heat capacity of Mg_3Sb_2 , Mg_3Bi_2 , and their alloys at high temperature. *Mater. Today Phys.* **6**, 83–88 (2018).
- Kresse, G. & Furthmüller, J. Efficient iterative schemes for ab initio total-energy calculations using a plane-wave basis set. *Phys. Rev. B* **54**, 11169–11186 (1996).
- Kresse, G. & Joubert, D. From ultrasoft pseudopotentials to the projector augmented-wave method. *Phys. Rev. B* **59**, 1758–1775 (1999).

55. Blöchl, P. E. Projector augmented-wave method. *Phys. Rev. B* **50**, 17953–17979 (1994).
56. Perdew, J. P., Burke, K. & Ernzerhof, M. Generalized gradient approximation made simple. *Phys. Rev. Lett.* **77**, 3865–3868 (1996).

Acknowledgements

This work was supported by the National Key Research and Development Program of China (2019YFA0704902), the National Science Fund for Distinguished Young Scholars (No. 51725102), the National Natural Science Foundation of China (Nos. 52101275, 51761135127), and the Deutsche Forschungsgemeinschaft (DFG, German Research Foundation)—Projektnummer (392228380).

Author contributions

A.L., C. Fu, and T.Z. designed the project. A.L. prepared the samples and carried out the transport measurements. A.L. characterized the crystals with input from Y.W. C.H. performed first-principles calculations. B.H. measured the thermal transport properties of single crystals. M.Y. carried out the angle-resolved photoemission spectroscopy study. X.Z. and C. Felser supervised the project. A.L. and C. Fu analyzed the data and wrote the original manuscript. All the authors reviewed and edited the manuscript.

Competing interests

The authors declare no competing interests.

Additional information

Supplementary information The online version contains supplementary material available at <https://doi.org/10.1038/s41467-021-25722-0>.

Correspondence and requests for materials should be addressed to Chenguang Fu or Tiejun Zhu.

Peer review information *Nature Communications* thanks the anonymous reviewer(s) for their contribution to the peer review of this work. Peer reviewer reports are available.

Reprints and permission information is available at <http://www.nature.com/reprints>

Publisher's note Springer Nature remains neutral with regard to jurisdictional claims in published maps and institutional affiliations.



Open Access This article is licensed under a Creative Commons Attribution 4.0 International License, which permits use, sharing, adaptation, distribution and reproduction in any medium or format, as long as you give appropriate credit to the original author(s) and the source, provide a link to the Creative Commons license, and indicate if changes were made. The images or other third party material in this article are included in the article's Creative Commons license, unless indicated otherwise in a credit line to the material. If material is not included in the article's Creative Commons license and your intended use is not permitted by statutory regulation or exceeds the permitted use, you will need to obtain permission directly from the copyright holder. To view a copy of this license, visit <http://creativecommons.org/licenses/by/4.0/>.

© The Author(s) 2021